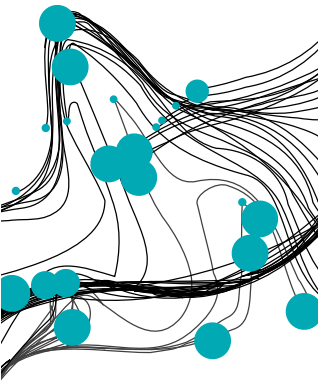

RAM ROBOTICS AND MECHATRONICS

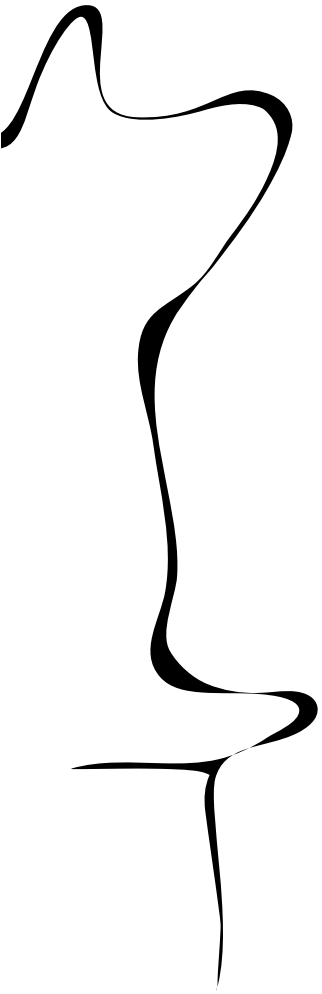

FORCE-BASED MEASUREMENT OF TISSUE STIFFNESS IN 1-DOF NEEDLE INSERTION ROBOTIC DEVICE FOR LIVER INTERVENTIONS

M. (Manaswini) Motheram

MSC ASSIGNMENT

Committee:
dr. ir. M. Abayazid
M.S. Selim, MSc
dr. ir. C. Salm

October, 2023

047RaM2023
Robotics and Mechatronics
EEMCS
University of Twente
P.O. Box 217
7500 AE Enschede
The Netherlands

UNIVERSITY OF TWENTE. | TECHMED CENTRE
UNIVERSITY OF TWENTE. | DIGITAL SOCIETY INSTITUTE

Abstract

The field of medical robotics has witnessed a surge in the application of needle insertion robots for tumor diagnosis and treatment. Traditionally, these systems predominantly rely on image guidance for tumor localization, which often results in extended procedure durations and can potentially cause side effects, such as excessive exposure to radiation from CT scans. This research proposes an innovative approach that estimates tumor stiffness based on the forces experienced during needle insertion, thereby reducing the dependence on imaging. A one-degree-of-freedom (1-DOF) needle insertion robot is designed for this purpose. To facilitate realistic testing, a liver phantom with varying tumor stiffnesses is developed, designed to closely emulate the properties of a human liver and its tumors. The robot conducts a series of experiments, inserting a needle into the phantom which contains single and double tumors. A force sensor attached to the needle records the forces experienced during each insertion. This approach could potentially lead to more efficient methods for tumor detection and treatment, reducing the reliance on imaging and thereby minimizing the associated drawbacks. The study also delves into the design and functioning of the robot, ensuring it is user-friendly and intuitive. Preliminary dry runs were conducted to ascertain contact forces, which were then employed as an offset during the needle insertion procedure. The integration of the force sensor with the needle is of paramount importance in the design. The study also investigates the influence of the material composition of the liver phantom on force readings by comparing two phantoms made of different materials, ecoflex and gelatin. The results provide insights into tissue stiffness and the complex interaction of forces during needle insertion, laying the groundwork for further study and improvements to current procedures. Ultimately, this approach could be a valuable resource for comprehending and improving needle insertion techniques.

Contents

Chapter 1

Introduction

Given the prevalence of liver tumors worldwide, early and accurate detection of these tumors has also become a critical area of focus in the medical field. Early detection can significantly improve a patient's chances of overcoming the disease. One of the most common site for carcinogenic tumors as well as non-carcinogenic tumors is the liver, which has therefore gained substantial attention from researchers in the field [1]. The complexities associated with liver-related medical interventions are diverse. These challenges include: the difficulty of early detection due to the lack of specific symptoms, the possibility of misdiagnosis due to the complicated structure of the liver, the risk for quickly spreading tumors, and the difficulties of various treatment options, such as surgery, chemotherapy, and radiation therapy. Moreover, individuals diagnosed with liver cancer often face a challenging prognosis. These challenges point to the urgency of improving the diagnostic and treatment methods, thus adding to the relevance of this research [2]. Amidst these challenges, advancements in other medical areas offer potential solutions.

In recent years, designing and creating robotic systems for medical operations have garnered significant interest. As needle insertion operations typically require high level of precision and accuracy to avoid damaging vital organs or tissues, many current insertion techniques concentrate on developing robots, particularly for these procedures. These needle insertion robots have proved crucial in the context of hepatic biopsies and medical applications. Liver biopsy is one of the main techniques that incorporates needle insertion robots for liver tumors diagnosis [3]. With the current advancements in medical robots, surgeries have transformed to provide more accuracy, minimal invasiveness, and being less tremor-prone [4].

1.1 Problem Statement

In the practice of medicine, an accurate assessment of tissue stiffness can be crucial for diagnosis, treatment planning as well as monitoring [5]. Clinical practitioners have traditionally relied on palpation or imaging techniques to assess tissue stiffness [6]. However, these methods often lack the precision necessary to capture the intricate mechanical properties of tissues [7]. This lack of precision can lead to potential tissue damage during needle insertions. During surgical procedures, a surgeon's tactile feedback, may not always capture the nuanced variations in tissue properties.

Various types of image guided techniques are used for tumor detection in the medical field. However, these procedures can be ineffective and error prone because of the two dimensional nature of the scans generated as well as the time taken for these scans [8]. Additionally, while inserting the needle, the computational load and picture quality variations during the image guided procedures, may result in tissue injury or trauma [9]. It should also be noted that one of the primary image guiding techniques, the Computed Tomography (CT) Scan [10], exposes the patient to an excessive amount of radiation throughout the process and lacks real-time feedback [11]. A surgeon using needle insertion method can avoid exposure to radiation by reducing the number of scans and relying more on force feedback required for the treatment. This adds to the significance of this research.

Elaborating on the challenge mentioned earlier, in image-guided needle biopsy procedures, it is difficult to sense the subtle changes of forces applied to the needle upon contact with the tissue that are difficult to be identified by the physician. These challenges point to a clear need for a more precise method. A potential solution is a robot that performs needle insertions and measures the force to assess the tumor's stiffness. However, this strategy has not been extensively studied.

This study aims to fill this gap by investigating the use of a needle insertion robot to measure the forces between the needle and the tissue during insertion. The forces are also evaluated to estimate the stiffness of these tumors. Overall, this thesis delves into the exploration of tumor stiffness in relation to these forces. It presents a method for determining this stiffness, and includes an examination of how force behavior changes when varying stiffness is present in the liver.

1.2 Proposed Study

Most of the research about needle insertion robots heavily rely on image guidance to accurately locate and target tumors. This dependence on imaging can lead to patient trauma, extended procedure times, and increased costs. The proposed study aims to explore an alternative approach to tumor detection using a needle insertion robot. Specifically to investigate the possibility of detecting tumors and determining their mechanical properties based on the forces experienced during needle insertion, without the need for image guidance.

This research aims to advance minimally invasive surgery by integrating force sensors for enhanced tumor detection and treatment as discussed in [12]. These procedures have revolutionized surgeries making them more reliable [13] [14]. This study proposes, designing and developing of a one degree-of-freedom (1-DOF) needle insertion robot with integrated force sensing. For the purpose of the experimental testing, a liver phantom with varying stiffness is fabricated to closely mimic the properties of a real human liver and tumors. Different experiments will involve the robot penetrating through this phantom, with a force sensor recording exerted forces during insertions. The primary aim of this research is to explore the potential use of force sensors in tumor detection by reducing the reliance on imaging and thereby minimizing the associated drawbacks. Challenges and limitations of this approach will be analyzed. The integration of force sensors in robotic systems promises enhanced medical procedure efficacy and safety, enabling real-time tissue identification and revolutionizing surgical interventions.

1.3 Research Question

Based on the problem statement, this study aims to focus on the following main research question:
How can forces be utilized to measure the variation in different tissue stiffness during a 1 DOF needle insertion procedure in a slave configuration system for liver interventions?
The main research question is further elaborated by the following related sub-research questions:

- How efficiently does the 1-DOF device recognize different materials within a healthy tissue of the liver?

- How does the material composition of the liver phantom influence the force readings obtained by the 1-DOF needle insertion robot?
- How does the proposed approach detect successive changes in material during single insertion?

1.4 Overview of the thesis structure

This thesis is composed of six major chapters, followed by a references and appendices. Chapter 2 presents a thorough overview of relevant theories and research, highlighting tumor detection methodologies, robotic needle insertion systems with force sensing, and liver phantom studies. Chapter 3 details the design of the 1-DOF robot, the fabrication of the phantom with tumors, and delves into the mathematical model for the forces. This is followed by Chapter 4, which outlines the experimental setup and procedure. The subsequent chapters present the findings and implications of the study. Chapter 5 then presents the discussion of the results. Finally, Chapter 6, serves as the conclusion, summarizing the key findings and their implications as well as the future scope of this research. Each chapter contributes to the overall narrative and findings of the thesis, ensuring a comprehensive exploration of the research question.

Chapter 2

Literature Review

This chapter covers a comprehensive review of previous research and literature in the domain of needle insertion using force-sensing capabilities for tumor detection. As the focus of this research is on a robotic device designed for tumor detection through needle insertion, the literature emphasizes tumor detection methodologies and state-of-the-art robotic systems equipped with force-sensing capabilities. The research also highlights the fabrication of liver phantoms and the significance of their use in simulating real-life scenarios for testing.

2.1 Tumor Detection Methods

As discussed in Chapter 1, over the past few years, various procedures and techniques for liver tumor detection and characterization have been developed. The imaging tests that are used for liver tumor diagnose can be broadly classified into three categories: Ultrasound (US), CT Scan, and Magnetic Resonance Imaging (MRI) [15]. Ultrasound, is a non-invasive and widely available imaging technique which uses high-frequency sound waves to generate images to visualize and characterize liver tumors which is seen in figure 2.1 [16]. Francis A. Duck elucidates several challenges associated with ultrasound imaging, including heating, acoustic cavitation, gas-body effects, and radiation pressure [17]. In addition to this, ultrasound may not detect certain hepatic tumors due to their diminutive size, location, or echogenicity [18].

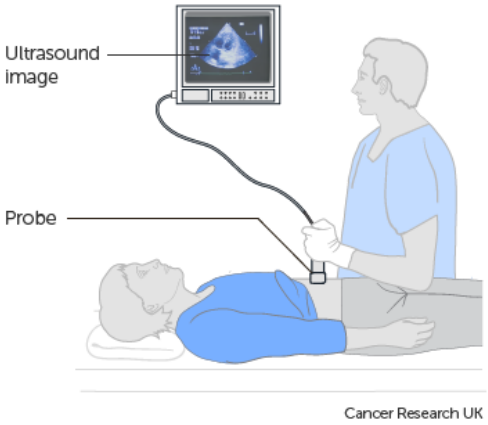

Figure 2.1: Ultrasound Scan [19]

CT Scan involves taking a scan of the liver where it uses an x-ray machine linked to a computer to capture detailed images of internal body areas. However, it also poses challenges related to extensive radiation exposure associated with CT Scan can do more harm than good in certain situations [20]. The detectability of liver tumors using CT scans decreases with reduced radiation doses from standard to low levels. This was observed in a study, which highlighted the case of a 65-year-old woman with a typical BMI diagnosed with a 0.9 cm Hepatocellular Carcinoma (HCC) [21]. While the tumor in this case was identifiable in both standard and low-dose CT scans, it remained undetected in ultra-low-dose scans. Such findings, illustrated in figure 2.2, suggest that even moderate size malignancies like a 0.9-cm hepatocellular carcinoma can elude detection in ultra-low-dose scans, underscoring the limitations of CT scans at higher radiation levels and potential overexposure risks.

Another commonly employed image guidance method, MRI, uses magnetic fields and radio waves to produce high-resolution images of the liver, enabling the detection, characterization, and monitoring of tumors. However, the strong magnetic field, radio frequency signal interactions, and rapidly changing gradients in the MRI environment present significant challenges for the development of MRI-compatible robots [22]. Despite its accuracy, the procedure can be lengthy because it involves an iterative process. In this process, the needle is incrementally moved towards the target lesion, with multiple scans taken to verify its position, requiring occasional adjustments of the needle's position [23] [24] [25]. This method, combined with possible

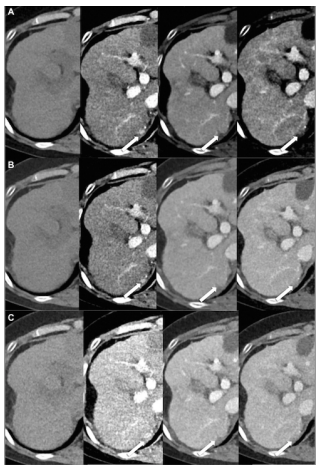

Figure 2.2: CT Scan of liver with HCC [21]

disturbances from patient motion and the extended time of the procedure, can impact patient ease and adherence, and the significant expense poses an additional challenge.

2.2 State of Art

In this section, five state of art needle insertion robots along with the key components from literature are presented. In the development and application of force sensing and control techniques for robot-assisted needle insertion, Yang et al. conducted a survey on force feedback and control, discussing various techniques for modeling, identifying, and controlling the forces involved [26]. These advancements aim to minimize tissue deformation and needle deflection while providing the operating surgeon with a direct sensation of operation and control over the surgical tools. In this paper, Yang et al. proposed a force feedback control approach for robotically guiding a needle into layered soft tissues [27]. They integrated a fiber optic force sensor at the needle tip to provide feedback to the control system during needle insertion as shown in figure 2.3. Using the wavelet transform approach, they analyzed the interaction force patterns with different types of soft tissues. Experimental tests were conducted on a phantom of porcine belly tissue with different layers of tissue which can be seen in figure 2.4, comparing the outcomes with and without force feedback. The results showed that the feedback strategy reduced insertion force, thus minimizing tissue deformation or damage.

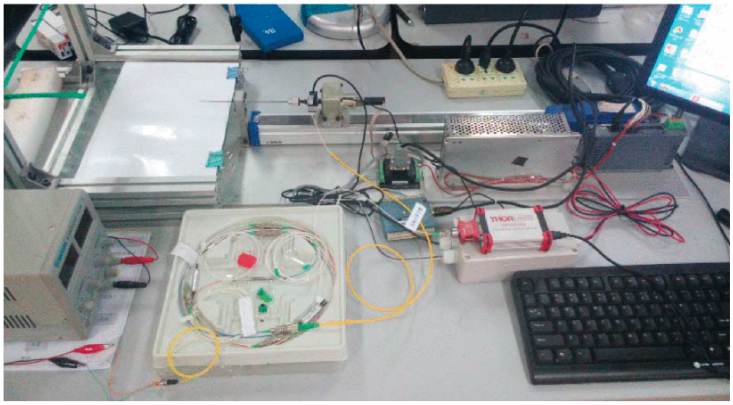

Figure 2.3: Needle insertion robot by Tangwen Yang et al. [27]

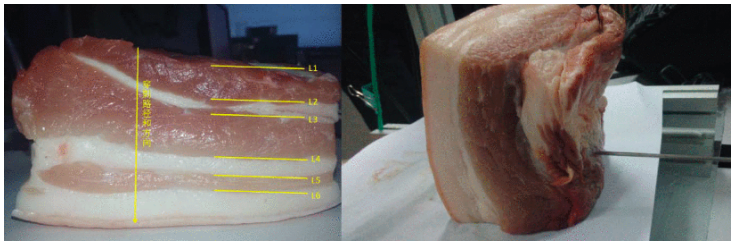

Figure 2.4: Porcine belly tissue [27]

In contrast to using a force sensor at the base of the needle, Washio et al. attached a pair of coaxial sensors to the needle and sheath to observe changes in the force profile, enabling the detection of the needle puncture with high sensitivity and robustness [28]. This method also provided the distinct advantage of enabling the sensor to differentiate between forces exerted at the needle's tip and those along its shaft. The authors conducted experiments to validate the sensor's performance, testing its puncture detection specificity under cardiac and respiratory movements and comparing its sensitivity with subjective experience using video-based detection. The sensor demonstrated higher sensitivity, even detecting instances of penetration that the surgeon could not properly identify.

Similarly, Zhang et al. proposed investigating the forces involved during needle insertion and determining the position between the needle tip and a nerve during ultrasound-guided regional anesthesia [29]. They utilized an annular force sensor clamped on a mount with the needle as well as a Direct Current(DC) motor shown in figure 2.5, for the needle insertion to conduct tests on lamb shanks. Although no discernible variation in force was observed

among different insertion speeds, future work will focus on conducting tests across a wider range of insertion speeds and exploring needle deflection and tissue deformation to enhance the understanding of needle-tissue interaction.

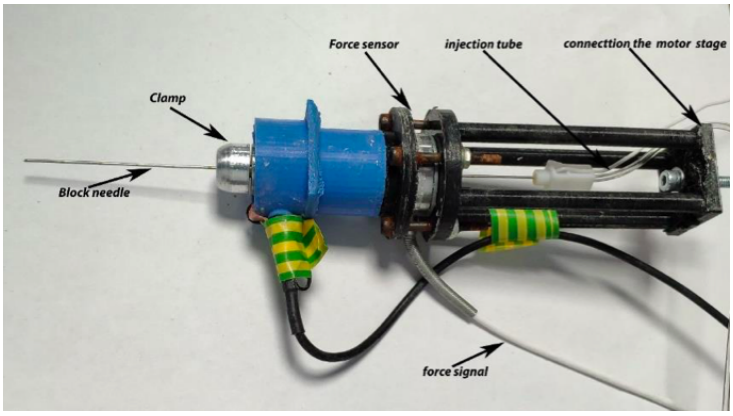

Figure 2.5: Force sensor setup by Zhang et al. [29]

In a different approach, Rossa et al. suggested a novel data-driven method for determining needle deflection in soft tissues [30]. Instead of traditional global modeling, they relied on local data collected from needle-tissue interactions during multiple insertions in ex-vivo tissue. To alter the direction of the needle bevel angle, a geared DC motor is used to spin the force sensor and needle axially. They utilized a JR3 Inc 6-DOF force/torque sensor suitable for their purpose which has also been used by Lehmann et al in [31]. In this paper, a method for detecting the route and rotation depth of a needle tip during insertion into soft tissue is presented. This method does not rely on image feedback and uses a kinematic cycling model instead. The authors provide a way to precisely control and monitor the needle's motions in real-time using the force sensor based deflection estimator where the needle insertion is done by DC motors which is shown in 2.6.

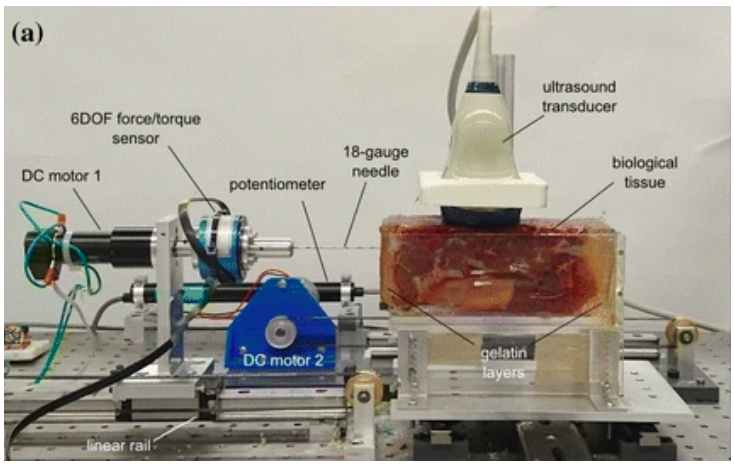

Figure 2.6: Needle insertion robot by Lehmann et al. [31]

Authors in [12] conducted a study to test an automated laparoscopic grasper using a haptic feedback device and a camera. They wanted to investigate the accuracy of visual feedback and force feedback in identifying the tissue hardness. The study involved testing multiple subjects, and the results showed that force feedback was more accurate than visual feedback in identifying tissue hardness. Literature existing showing that the maximum estimated force during tissue penetration is 0.715 N [32].

2.3 Liver phantom

Nonalcoholic Fatty Liver Disease (NAFLD) is a prevalent and widespread chronic liver condition that may lead to severe liver complications like cirrhosis and HCC [33] [34] [35]. The most reliable method for diagnosing and determining the severity of fibrosis in patients with nonalcholic steatohepatitis (NASH), historically has been liver biopsy [36] [37]. Another study explores the relationship between liver diseases and changes in liver tissue stiffness [38], particularly focusing on HCC. Which is the most common form of liver cancer, which often develops in a cirrhotic liver. The paper provides a range of liver stiffness values corresponding to different stages of liver diseases, ranging from normal to F4 fibrosis. The stiffness values range from 6kPa to 12.5kPa. These findings suggest that certain liver diseases can cause an increase in liver stiffness, potentially indicating advanced liver cirrhosis when stiffness values reach 12.5kPa or higher.

Liver phantoms are essential for studying liver diseases and to ensure the quality of diagnostic instruments by closely mimicking human tissue

characteristics. The liver phantom in [39] is made using a two-component flexible foam called FlexFoam III from Smooth-On. He et al. also explains the fabrication of a liver phantom using Ecoflex which is used for palpation, a silicone-based material, which closely mimics the mechanical properties of a real liver [40] which can be seen in 2.7. Such phantoms provide medical professionals with a realistic training tool. They can practice diagnosing liver disorders without patient risk, benefiting from the phantom's tactile properties that resemble an actual liver. The thoughtful design of these synthetic materials is emphasized in [41], highlighting the importance of accurately replicating human tissue. Additionally, in [42], a 10% wt gelatin-based liver phantom was made to evaluate the performance of the developed medical probe. In this study, the Young's modulus of the gelatin was found to approximate that of a healthy liver, as supported by [43].

Figure 2.7: Liver phantom by He et al. [40]

Chapter 3

Methods and Materials

Recapitulating the problem statement and the proposed study delineated in the preceding chapter 1, it becomes imperative to ascertain whether the mechanical properties of the tumor can be deduced from the exerted forces. To address the problem, an appropriate model is required. The designing and implementation of a 1-DOF needle insertion robotic device is discussed in this chapter. Furthermore, this chapter delves into the intricate process of fabricating the phantom. Subsequently a comprehensive overview of the experimental setup is provided.

3.1 Design and Implementation of the 1-DOF Robotic Device

In this section, a 1-DOF needle insertion robotic device, integrated with a force sensor is developed for measuring tissue stiffness.

3.1.1 Design Requirements

This section deals with the design requirements and the specifications of the robotic device.

- **Force required:** The puncturing force required for healthy human liver tissue usually ranges between 0.1 and 0.65 Newton (N) [44]. However, the phantom is designed to mimic the human liver with tumors. These tumors increase the need for a higher puncturing force. Considering the properties of these tumors, a sensor with maximum force of 10 N should be selected.

- **Stroke length:** The average size of the human liver is 7 cm for women and 10.5 cm for men [45]. The motor with a stroke length of 63.5 mm was selected to ensure that the length was sufficient to pierce the liver and also checking the availability of motor's with appropriate stroke length in market.
- **Reliable force readings:** It is essential to ensure consistency in force measurements for accuracy and reliability. Ideally, force measurements should have an accuracy of $\pm 1\%$ and a precision of $\pm 0.2\%$ to guarantee reliable tumor detection. Fluctuations or inconsistencies outside these ranges can introduce noise, potentially compromising the accuracy of tumor detection.
- **Minimize friction on the needle:** In order to prevent readings from being distorted by external resistances, it is important to ensure that the friction during the needle insertion process is minimized. It's also imperative to keep the friction within a limit of 15% of the force sensor's maximum load to ensure optimal performance by mostly detecting needle-tissue interaction forces and a more efficient design.
- **Minimize needle deflection:** To ensure the procedure's effectiveness of accurately targeting tumors while simultaneously protecting the surrounding healthy tissues from damage, it's crucial to minimize needle deflection.

3.1.2 Design Choices

To ensure the robot's effectiveness and uphold the safety and precision of its operations, considering the design requirements mentioned above, the subsequent design choices were made.

1. Given the varied puncturing forces, the robot was equipped with a Piezoresistive-based Honeywell FSA Series analog force sensor with a 10 N capacity.
2. A Portescap linear actuator stepper motor with a 63.5 mm stroke length for effective penetration was used for the robotic device to ensure precision and ease of control that tumors within the liver tissue is reached..
3. For the robotic device's needle insertions, an 18-gauge Aurora 5-DOF needle which is commonly used for biopsies was chosen which is shown in Figure 3.1.

Figure 3.1: Needle used for the design [46]

Specifications for these components are discussed in the following Table 3.1.

Table 3.1: Components Specifications

Specification	**Force Sensor**	**Motor**	**Needle**
Type	Piezoresistive	Linear Actuator Stepper Motor	Biopsy Bevel Tip
Operating Voltage	5V	5V	N/A
Measurement Range	0 - 10N	0 - 10N	18 guage
Accuracy	±3%	±1 Step	N/A

3.2 1-DOF Needle Insertion Device

The design and development phase incorporates the design requirements and choices. It's crucial to assess the actuator's compatibility, placement, and the integration of the force sensor and needle. The base support for the robotic device, shown in Figure 3.2 with dimensions, determined by the needle's length (170 mm) and the actuator's stroke length. To ensure linear movement with minimal friction, a metal rail guide with an linear carriage is employed. The force sensor's integration necessitated a specially designed mount, allowing sensor wires to connect easily to the Arduino board.

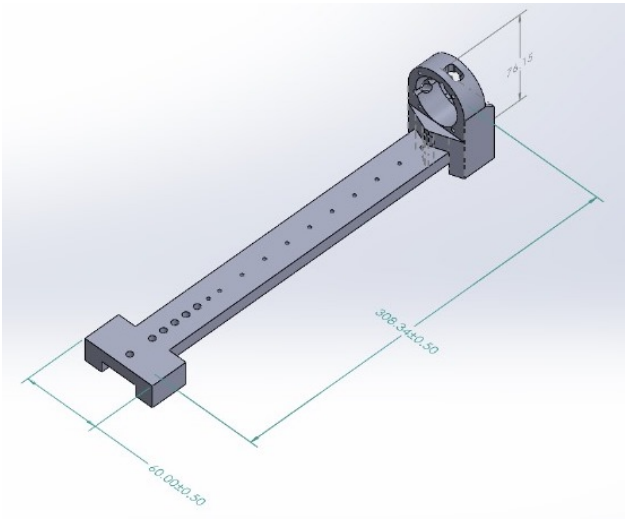

Figure 3.2: Base support for the device

A critical aspect of the design is the connection between the force sensor mount and the needle base. Directly connecting the needle to the sensor could introduce inaccuracies in force readings due to potential deflections or vibrations. Moreover, if adhesives are used to secure the needle, they could flex under pressure, producing results that are only partially accurate. To address this, a clamp joint, highlighted in blue in figure 3.4 was introduced between the force sensor mount and the needle base which protects the needle and provides a stable connection, as depicted in figures 3.3 and 3.4.

Given the needle's length, a support near its tip was essential to prevent excessive bending and target deflection. However, initial designs using certain 3D materials such as breakaway white, posed friction concerns, potentially damaging the needle. This was addressed by adjusting the design to minimize friction between the needle and its support. Additionally, the diameter of

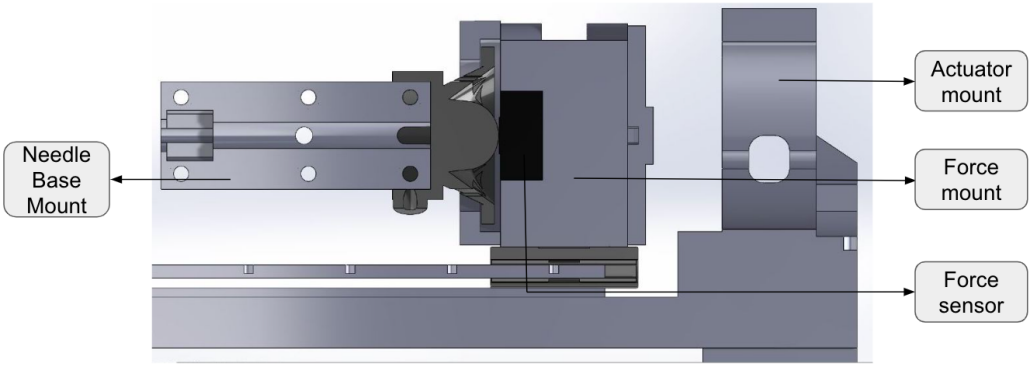

Figure 3.3: Cross sectional view of the clamp joint

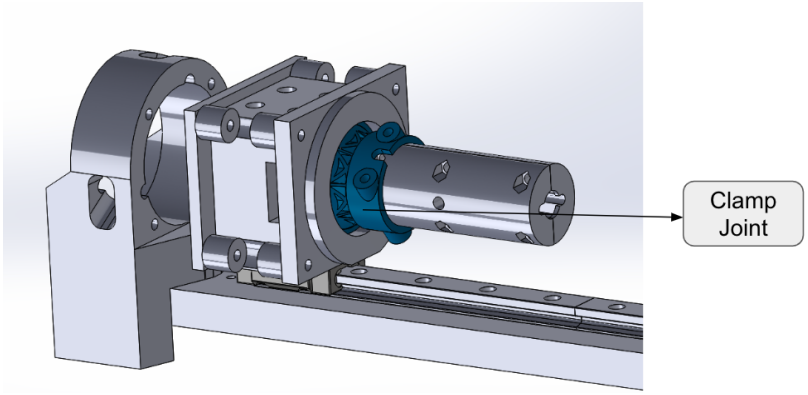

Figure 3.4: Flexible clamp joint

the needle support was increased to provide clearance beyond the needle's diameter, ensuring movement without friction. The modified needle support is shown in Figure 3.5 with the dimensions given in the figure in 'mm' units. The needle insertion robot was designed in Solidworks. This can be seen in Figure 3.6. This model was subsequently converted to an STL file for 3D printing. While Tough PLA was used for most parts, the clamp joint was crafted from Agilus. The final prototype of the robotic device is depicted in Figure 3.7.

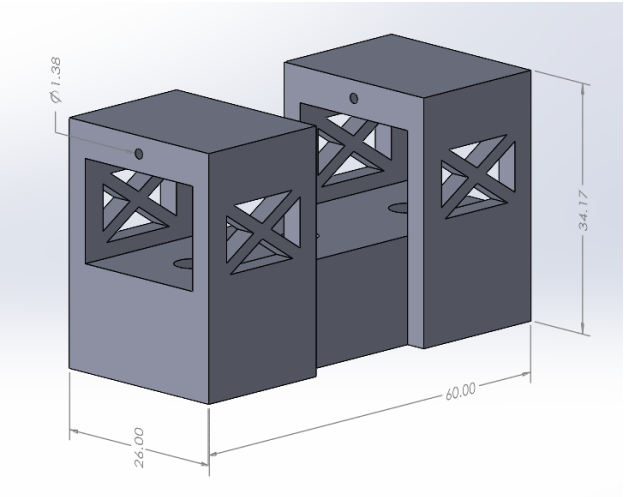

Figure 3.5: Needle support

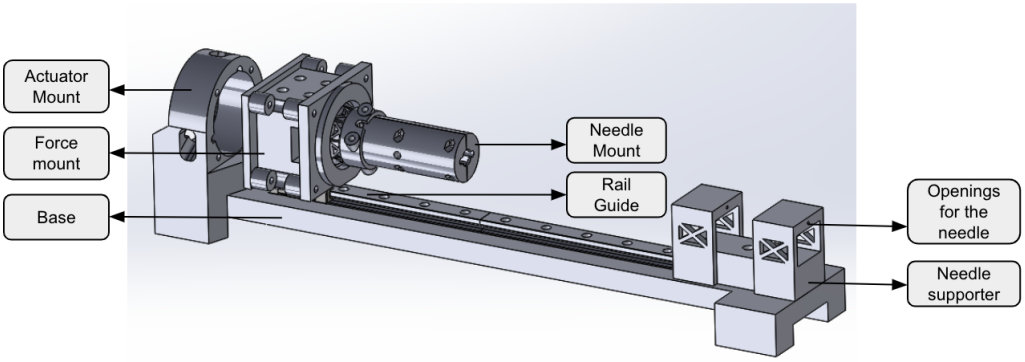

Figure 3.6: Robotic device simulated model

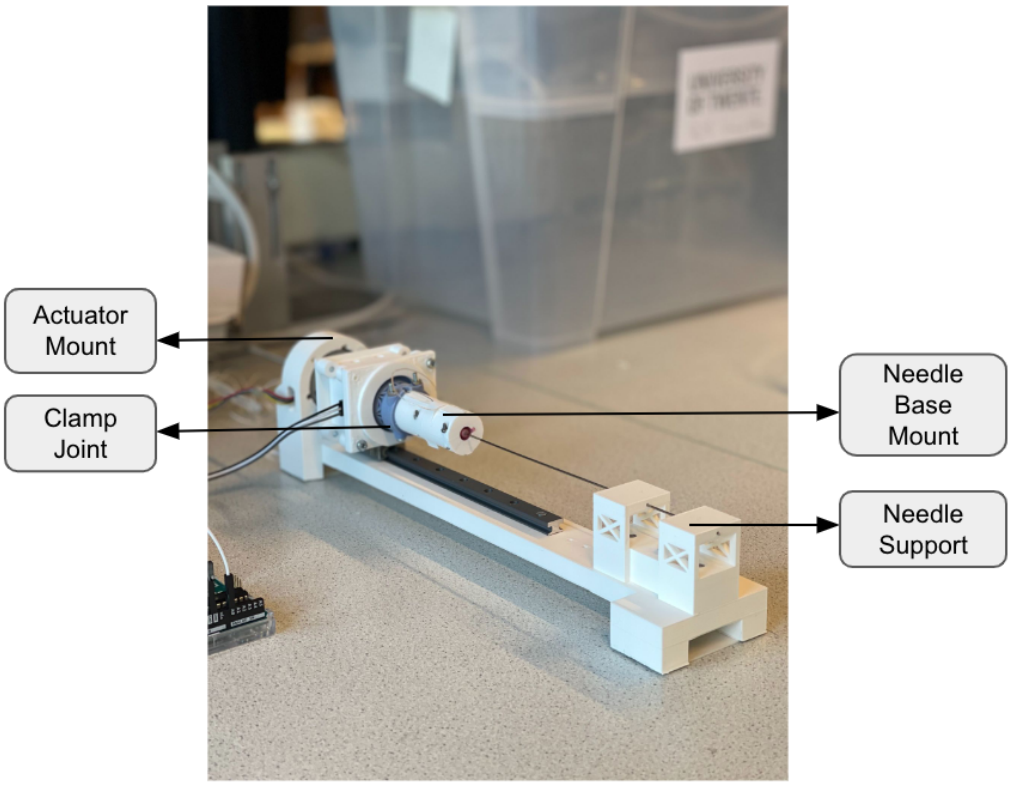

Figure 3.7: 1-DOF needle insertion robotic device

3.3 Development of the Liver Phantom

Employing a liver phantom that mimics varying tumor stiffnesses is essential for needle insertion experiments. The first step was to develop a compact phantom that closely mirrors the mechanical properties of a healthy human liver. Based on the literature, two such phantoms were crafted, as detailed below.

3.3.1 Silicon Phantom

A liver phantom can be fabricated using a mixture of Ecoflex 10 and slacker in a 2:1:1 (Slacker: Ecoflex 00-10 A: Ecoflex 00-10 B) ratio [40]. A small phantom was fabricated with these mechanical properties which can be seen in Figure 3.8.

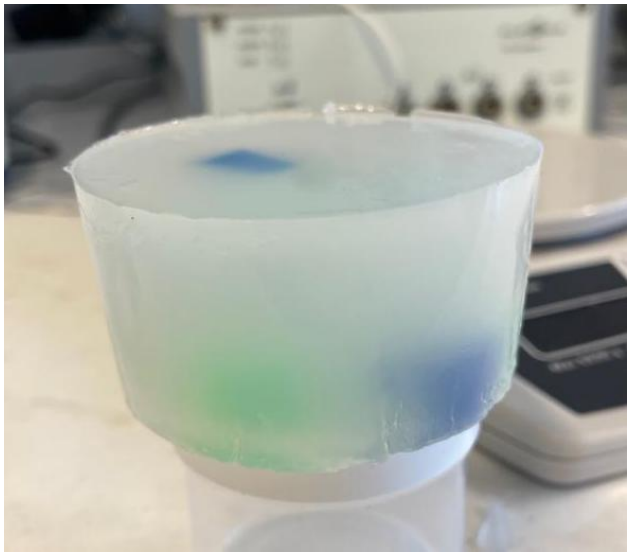

Figure 3.8: Fabricated Phantom

The next consideration was stiffness of the tumors. As outlined in Chapter 2, the stiffness of F4 fibrosis tumors typically starts from more than 12.5kPa [38]. To replicate this in the phantom, materials complying with this value, specifically Ecoflex 30 and 50, were used to create artificial tumors [47]. The psi values of the Ecoflex and their conversions to kPa are given in table 3.2.

Material	**Mixed Viscosity (in Centipoise(cps))**	**100 % Modulus (in psi)**	**100 % Modulus (in kPa)**
Ecoflex 00-30	3000 cps	10	68.9476
Ecolfex 00-50	5000 cps	12	82.7371

Table 3.2: Material Stiffnesses

Here, the Modulus 100 % refers to the stress at which a material has undergone 100 % of it's initial length of deformation. This can be viewed as the Young's Modulus, which gives a measure of material's stiffness under these particular conditions. The four fabricated tumors were distributed throughout the phantom randomly. This setup allowed for a realistic simulation of needle insertion into a liver with varying tumor stiffnesses. Figure 3.9 displays the labelled phantom, which is embedded with small tumors depicted in blue and green colors.

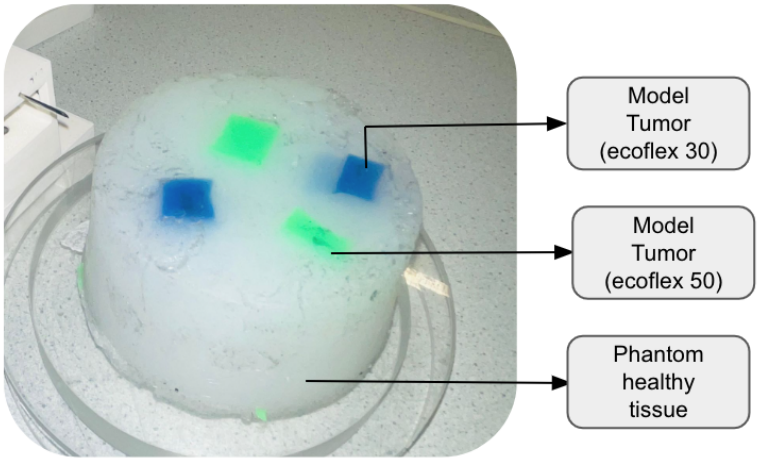

Figure 3.9: Liver Phantom

3.3.2 Gelatin Phantom

Due to the excessive stickiness of the ecoflex material liver phantom used in the previous section 3.3.1, it led to needle deflections which affected the

force readings during the presence of multiple tumors. A new phantom was fabricated using a different material. This phantom is composed of 10% wt gelatine, as recommended by [42]. A study suggests that the Young's modulus of this gelatine phantom closely resembles that of a healthy liver [43]. Similar to the previous phantom, ecoflex 30 (blue tumor) and ecoflex 50 (green tumor) were placed in this phantom during fabrication, shown in Figure 3.10.

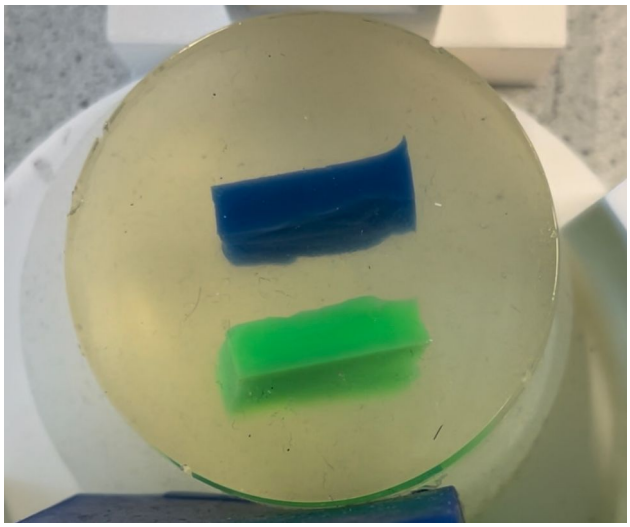

Figure 3.10: Phantom with Non-Adhesive Properties

3.4 Force Modeling

The stiffness of tumors in the phantom is calculated using interaction force measurements. To accurately represent needle insertion forces, it's essential to classify the data into stiffness, friction, and cutting forces. The forces are divided into 2 categories; design forces (F_{design}) and needle-tissue interaction forces ($F_{\text{needle, tissue}}$). The forces by the design as well as the needle-tissue forces are determined by the following equations:

$$F_{\text{design}} = F_{\text{clamp}} + F_{\text{friction, support}} \tag{3.1}$$

$$F_{\text{needle, tissue}} = F_{\text{friction, needle}} + F_{\text{stiffness}} + F_{\text{cutting}} + F_{\text{noise}} \tag{3.2}$$

Where, F_{clamp} denotes the contact forces at the clamp joint, $F_{\text{friction, support}}$ refers to the frictional forces on the needle support which is calculated in

section 4.2. While $F_{\text{friction, needle}}$ is the frictional forces on the needle while inserting through the phantom. $F_{\text{stiffness}}$ stands for the stiffness forces, F_{cutting} indicates the cutting forces, and F_{noise} accounts for external noises of the system.

3.4.1 Polynomial Regression Model

Understanding the correlation between penetration depth and the force due to tissue stiffness is vital. This relationship is especially complex due to the phantom being composed of two distinct materials, suggesting a non-linear interaction. To accurately calculate this complexity, a polynomial regression model is employed. The choice of a polynomial regression is driven by its ability to model non-linear relationships. This approach is particularly suited for representing needle insertion through regions with varied stiffness, as validated by Okamura [3]. The subsequent section provides a detailed mathematical representation of this regression model for the gelatin phantom.

$$f(x) = a_0 + a_1 x + a_2 x^2 + \cdots + a_{n-1} x^{n-1} + a_n x^n \tag{3.3}$$

Where f(x) represents the force exerted, x denotes the penetration depth and the coefficients are calculated from the experimental data in further sections. Upon differentiating the equation at a specific depth, the steepness of the curve can be determined, representing the material's mechanical properties, such as stiffness and damping. This value can be contrasted with another material to discern differences in tumor hardness.

3.4.2 Modified Karnopp Model

In the paper [3], the modified Karnopp model is employed to analyze frictional forces during needle insertion, distinguishing these from forces like stiffness and cutting. For this research, the aim is to precisely measure the frictional dynamics between the needle and the tissue throughout the insertion process. Based on the study's findings, the Karnopp model effectively captures these dynamics, making it a suitable framework for analysis. The modified Karnopp friction model is defined by following equations.

$$F_{\text{friction}}(\dot{z}, F_a) = \begin{cases} C_n sgn(\dot{z}) + b_n \dot{z}, & \dot{z} \leq -\Delta v/2 \\ max(D_n, F_a), & -\Delta v/2 < \dot{z} \leq 0 \\ min(D_p, F_a), & 0 < \dot{z} < \Delta v/2 \\ C_p sgn(\dot{z}) + b_p \dot{z}, & \dot{z} \geq \Delta v/2 \end{cases}$$

where: where C_n and C_p are negative and positive values of dynamic friction,
b_n and b_p are negative and positive damping coefficients,
D_n and D_p are negative and positive values of static friction,
$\dot{z}$ is the relative velocity between the needle and tissue,
$\frac{\Delta v}{2}$ is the value below which the velocity is considered to be zero,
and F_a is the sum of nonfrictional forces applied to the system. However, during the consistent movement of needle insertion, dynamic friction is the dominant force resisting its motion, so only dynamic friction is considered in this study.

Chapter 4

Experiments and Results

This chapter discusses the experiments involving the insertion of a biopsy needle into a liver phantom. The experiments took into account factors such as motor speed, needle position, and phantom orientation.

4.1 Experimental Setup

In this experiment, a the stepper motor was used, and a constant speed of 90 revolutions per minute (rpm) or 2.772 millimeters per second (mm/sec) was maintained for all of the experiments. The stepper motor, linked via a motor driver to the Arduino UNO, controls the needle's movement allowing for user-defined distance adjustments. Furthermore, it provides a detailed analysis of the results and outputs from each experiment, focusing on force assessment. The evaluation is organized into distinct subsections, each corresponding to a specific test, method, or experiment performed. To ensure reliability, each of the experiments was conducted three times.

4.2 Design Evaluation

Given the design requirements outlined in section 3.1.1, the needle insertion setup was incorporated within the specified design parameters to ensure comprehensive evaluation. The forces acting on the needle during insertion were calculated based on the details provided in section 3.4. Assessment was done for the following two cases:

1. The force exerted at the clamp joint
2. The frictional force at the needle support

The first case of the experiment focuses on evaluating the design in terms of clamp force (F_{clamp}) without any movement. The "clamp force" in this context refers to the force that was measured when the force sensor was connected to the needle through a clamp joint, as discussed in chapter 3.2. The contact force was calculated from the force-time graph when the stepper motor was stationary. This graph (as shown in the Figure 4.1) demonstrates variations in force levels between 1.07 N and 1.10 N over a period of 8.7 seconds. To minimize these variations and achieve a smoother representation of the data, a moving average filter was applied. In the assessment, the clamp force was measured over three iterations, all yielding similar force values with the needle maintained at the same position each time. The average force derived from these iterations was 1.082 N. This value effectively represents the force exerted at the clamp joint.

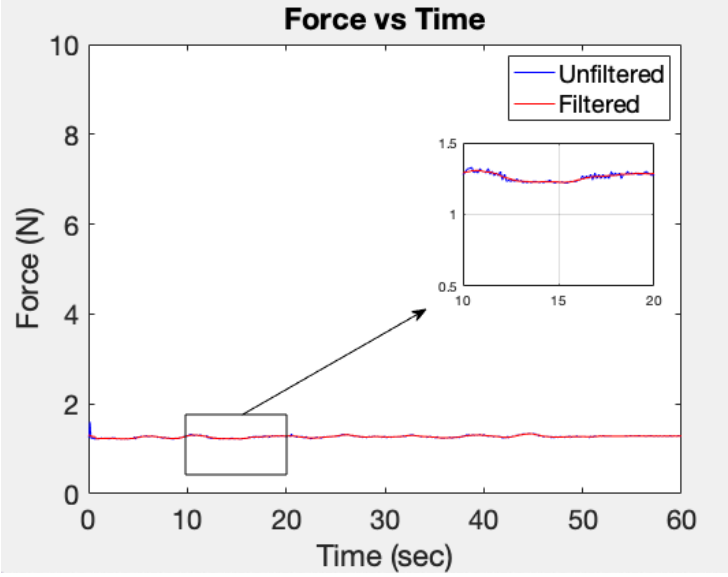

Figure 4.1: Force as a function of time graph without actuation with zoomed-in inset over a force range of 0.9 - 1.4 N

Due to the extended length of the needle, deflection occurs. And, to counteract this deflection, a needle support was introduced. However, this support introduced friction. It is crucial to analyze the frictional forces at the needle support to determine the extent of friction acting on the needle. The frictional force ($F_{frictional,needlesupport}$) values were calculated over time with no penetration of the needle into any material (dry run). This allowed to assess both, the performance of the needle support system under baseline

conditions and also the friction forces experienced by the needle at a specific speed. The relationship between force and time is illustrated by the graph in Figure 4.2 with an excerpt from it over the range of 0 - 0.4 N. It can be observed that the force varies between 0.048 N and 0.318 N over a time of 60 seconds.

This iteration for the dry run was conducted three times and similar value of the mean frictional force was achieved. The experimental frictional forces can be calculated as follows:

$$F_{\text{total}} = F_{\text{frictional, needle support}} + F_{\text{clamp}} \tag{4.1}$$

Where, F_{total} is the total force from the dry run and F_{clamp} is the clamp force. Using which, the computed mean force for the forward motion of the needle was 0.2335 N.

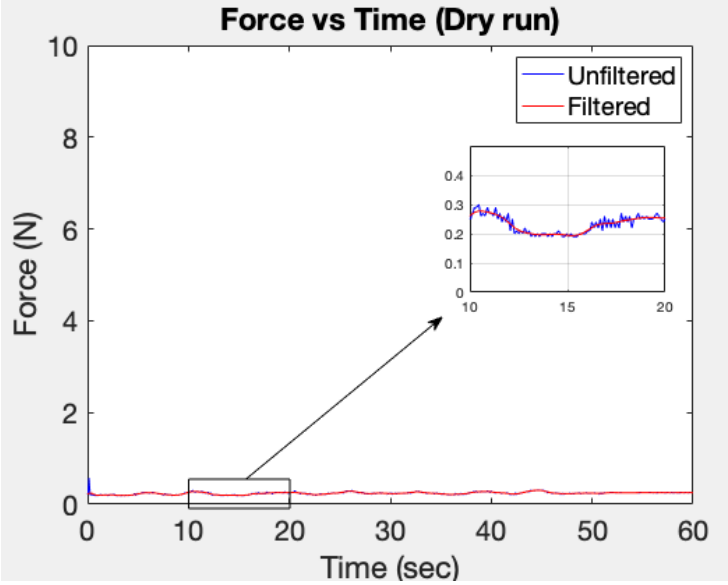

Figure 4.2: Force as a function of time graph during dry run with zoomed-in inset over a force range of 0 - 0.4 N

Here, the calculated clamp forces and frictional forces account to the force acting upon the needle and hence have been calculated. Both the forces experienced by the needle during the experiments was 1.3155 N.

The fabricated phantom's material closely mimics the biological tissue of human liver. Given the frequent interactions of the needle with ecoflex and gelatin, friction by the phantom on the needle which is the penetration

friction in this context has been set aside. Frictional forces at the needle support consistently impact the measurements. Through multiple tests with the same experimental setup and conditions, it was determined that the design forces amounted to 1.3155 N. To ensure accuracy in subsequent experiments, this force was estimated and then subtracted, effectively canceling out the design forces and focusing solely on the force exerted by the needle during penetration through the phantom.

4.3 Needle insertion through the fabricated tumors

To verify the force sensing capabilities of the device the needle insertion was carried out through two different materials with varying stiffnesses. For these insertions, forces were recorded and young's modulus was calculated. The two cases are shown below:

1. Fabricated Ecoflex 30 (blue) tumor
2. Fabricated Ecoflex 50 (green) tumor

To better comprehend the individual properties and stiffness of the tumors, separate tests were conducted on two fabricated tumors, each with dimensions of 37 mm, 74 mm, and 74 mm. The needle is allowed to penetrate with 30 mm for both of the two cases through the phantom and the forces are measured accordingly. The orientation of the phantom during these tests can be seen in Figure 4.3. For the initial test, the blue tumor was positioned perpendicular to the needle. The graph in Figure 4.4 displays the forces recorded as the needle entered the tumor. The moment of needle contact was marked with an arrow on the force vs position graph at approximately 4.2 mm. The force at this peak was noted to be 0.23 N at 7.4 seconds from the force vs time graph. It can be observed in Figure 4.4a, the forces increase exponentially from 0.23 N to 1.44 N. After reaching a peak of 1.44 N, the decrease in force values from 1.44 N to 1.31 N indicates that the phantom was undergoing relaxation, because the needle insertion was stopped after reaching the desired distance of 15 mm.

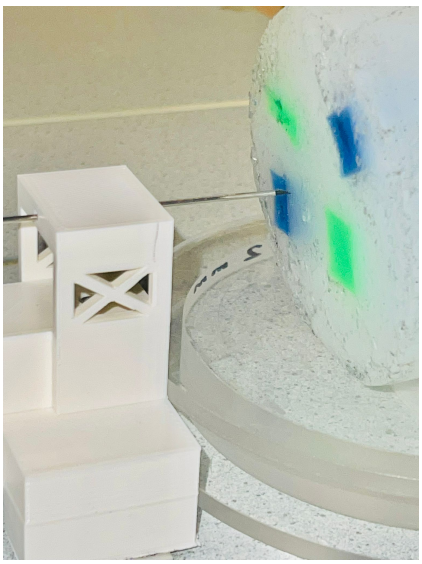

Figure 4.3: Phantom orientation during insertion

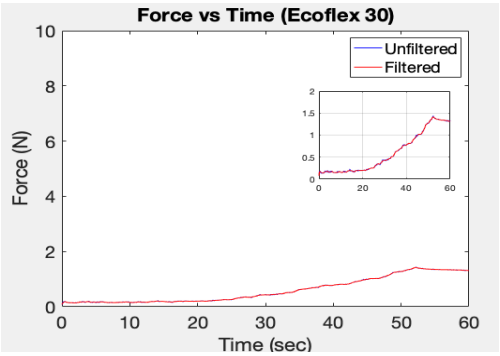

(a) Force vs. Time graph over a force range of 0 - 10 N with a zoomed-in inset with the same range.

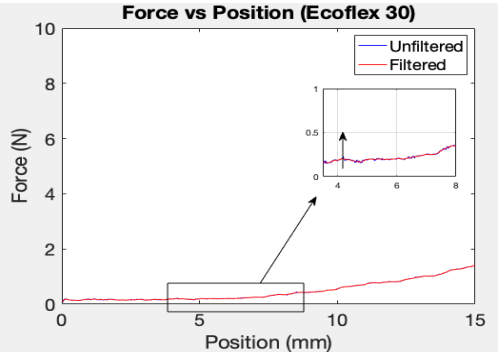

(b) Force vs. Position graph with a zoomed-in inset from 2 - 8 mm

Figure 4.4: Needle insertion through ecoflex 30 (blue).

A similar experiment was conducted on a single green tumor, and the corresponding forces were illustrated in Figure 4.5. In this case, the needle penetration occurred at the 4.15 mm, with a force of 0.26 N, as indicated in Figure 4.5b. The force at this peak is recorded as 0.26 N at 7.5 seconds on the force vs time graph. After reaching a maximum force of 1.96 N, the force values decreased to 1.86 N, indicating that the phantom was undergoing relaxation. This relaxation occurred because the needle insertion was halted after reaching the desired distance of 15 mm.

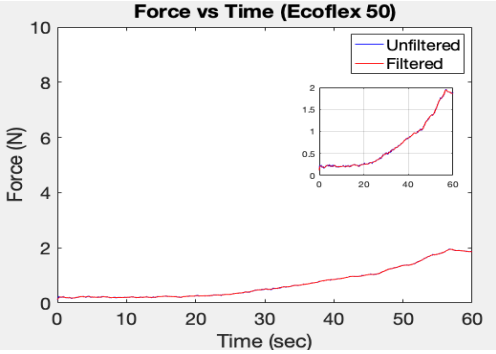

(a) Force vs. Time graph over a force range of 0 - 10 N with a zoomed-in inset with the same range.

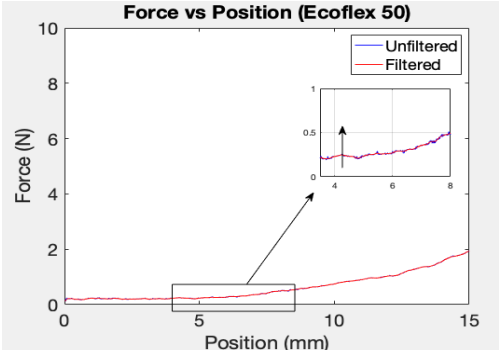

(b) Force vs. Position graph with a zoomed-in inset from 2 - 8 mm

Figure 4.5: Needle insertion through ecoflex 50 (green).

4.4 Needle insertion in Ecoflex phantom

In previous experiments, the primary emphasis was on assessing the stiffness of the individual fabricated tumor. However, in this section, variations in force measurements are calculated when the fabricated tumor is embedded within healthy tissue of the phantom. This setup allows for identifying differences in tumor stiffness, aligning with the research question mentioned in section 1.3. The needle insertion through the phantom was experimented for needle insertion through ecoflex 30 (blue) and ecoflex 50 (green) inside the healthy phantom.

Without any support on the phantom and due to the high penetrating force exerted by the needle, the phantom was pushed backward, preventing the needle from penetrating. Hence, it was necessary to secure the fabricated phantom to prevent this movement caused by needle insertion. A support structure shown in Figure 4.6 was designed to ensure the phantom remains stable, while also reducing deflection of the needle.

In the two cases mentioned above, the velocity was maintained constant, but the distance varied: it was set at 40 mm for the first case, and 45 mm for the second case as the tumor's placement varied inside the phantom which is manually calculated. The dimensions of the phantom were height: 37 mm

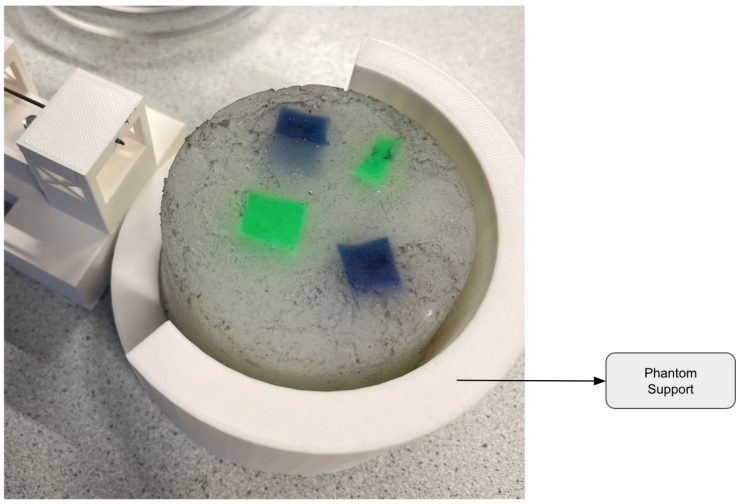

Figure 4.6: Phantom Setup

and diameters: a) 74 mm (top), b) 67.6 mm (bottom). In the first case, the experiment involved needle insertion through the blue tumor present in the phantom, and the measured forces are illustrated in Figure 4.7. The needle was inserted directly into the blue phantom, which was positioned perpendicular to the needle, with its flat surface facing the needle. The penetration into the blue tumor occurred at approximately 28 mm, at which point the force experienced was 1.452 N, as indicated on the force vs time graph in Figure 4.7b. Once the needle penetrated the blue tumor inside the phantom, the forces increased exponentially, resulting in a force of 2.922 N when the desired distance of 40 mm was reached. After the needle insertion is complete, the force observed reduces from 2.922 N to 2.722 N. This can also be observed in the both of the sub-graphs, where the position value remains constant and the force value decreases, signifying relaxation of the phantom which is seen in Figure 4.7a.

Similarly, the needle was inserted through a green tumor present in the phantom, and the recorded forces are illustrated in Figure 4.8. The force vs time graph marks the point of needle puncture through the tumor, indicating a peak force of 4.492 N experienced at approximately 29 mm. As the needle penetrates through the green tumor, the force begins to increase significantly until it reaches 6.362 N, at the desired distance of 45 mm. When the needle insertion is halted, the force decreases from 6.362 N to 5.952 N as the phantom undergoes relaxation which is seen in Figure 4.8a.

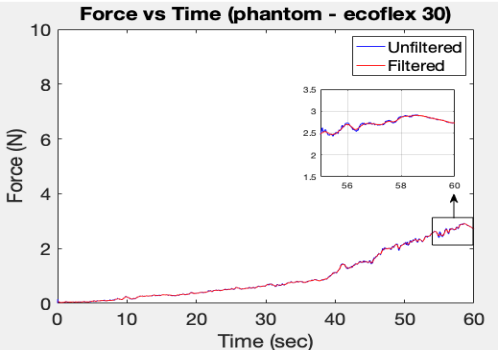

(a) Force vs. Time graph over a force range of 0 - 10 N with a zoomed-in inset with the same range.

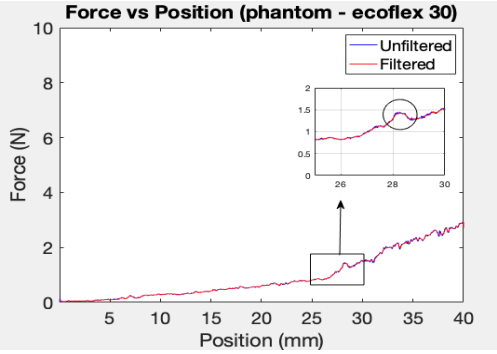

(b) Force vs. Position graph with a zoomed-in inset from 25 - 30 mm

Figure 4.7: Needle insertion through ecoflex 30 (blue) of the liver phantom.

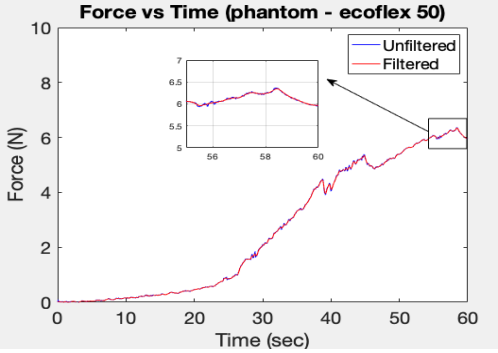

(a) Force vs. Time graph over a force range of 0 - 10 N with a zoomed-in inset with the same range.

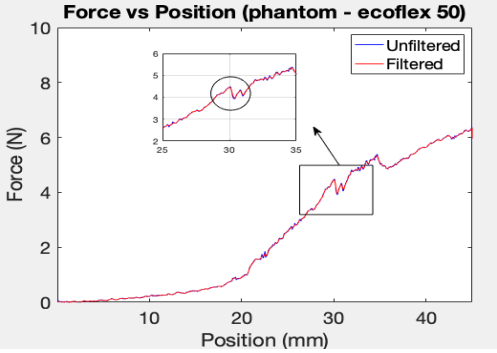

(b) Force vs. Position graph with a zoomed-in inset from 25 - 30 mm

Figure 4.8: Needle insertion through ecoflex 50 (green) of the liver phantom.

4.5 Needle insertion in Gelatin phantom

This section outlines the experimental procedure of needle insertion through a gelatin phantom embedded with two distinct tumors. A more refined phantom was developed, to address a sub-research question about successive changes in material during single needle insertion through the phantom. This was done to address the stickiness observed in the initial phantom, which caused deviations in the needle's trajectory during deeper penetrations, leading to inaccuracies in force readings.

While the control parameters employed for this experiment are consistent

with those of previous tests, the penetration distance was adjusted to 50 mm to reflect the phantom's width. The corresponding force-time graph for this specific experiment is illustrated in Figure 4.9. The peaks observed in the graph indicate the moments when the needle traversed the tumors. The first peak shows a maximum force of 1.038 N at 50.1 seconds at the instance the needle exited the blue tumor, followed by a force of 0.748 N at 50.88 seconds, recorded after the needle had exited the blue tumor (show in Figure 4.10). Before entering the blue tumor, the needle passed through the healthy tissue. During this phase, the forces exerted on the needle were insignificant, remaining constant around 0.16 N, and they can therefore be neglected. Once the needle traversed the first blue tumor, it re-entered the healthy tissue. From 51 seconds to 56 seconds, the forces remained consistent around 0.16 N, as the healthy tissue offers less resistance than the tumor tissue. The second peak, associated with the second tumor, shows a maximum force of 2.588 N at 75.61 seconds (show in Figure 4.11). When the needle penetrated through the green tumor, the peak force recorded at 77.87 seconds was 1.88 N.

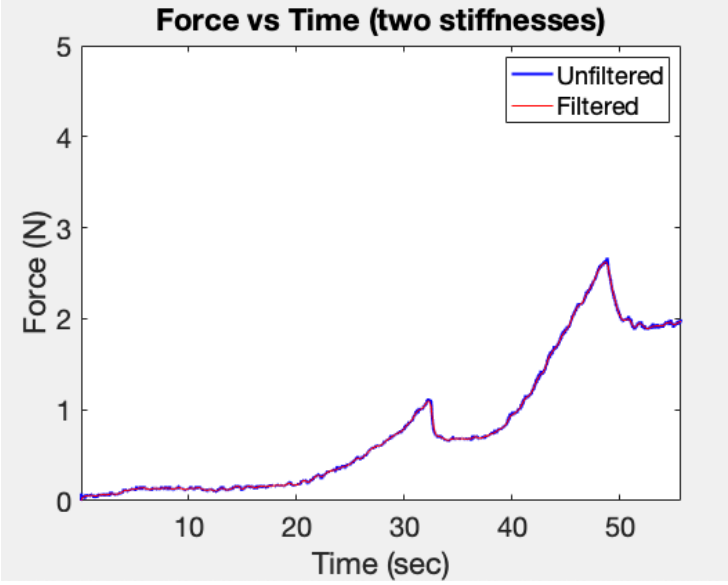

Figure 4.9: Force vs. Position graph over a force range of 0 - 10 N, needle insertion through two stiffnesses of the gelatin liver phantom.

The relationship between the force exerted and the insertion depth of the needle for the blue tumor is depicted in Figure 4.12, while the relationship for the green tumor is illustrated in Figure 4.13. For the blue tumor, the

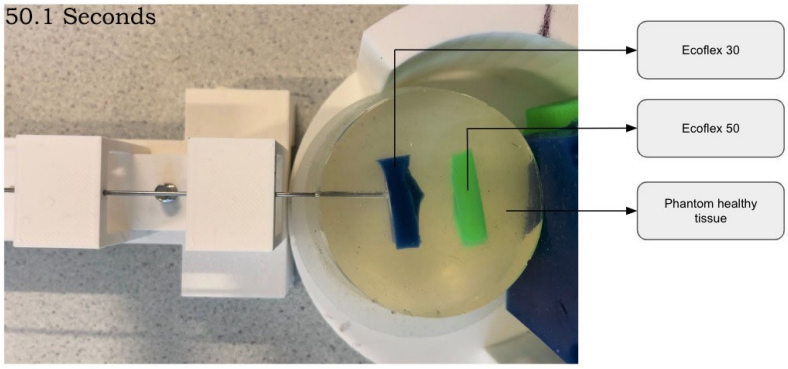

Figure 4.10: Needle traversing through the Ecoflex 30 (blue) tumor

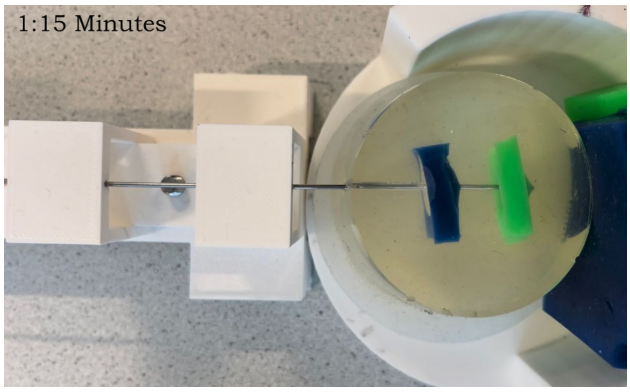

Figure 4.11: Needle traversing through the Ecoflex 50 (green) tumor

needle contact on the surface was at a depth of 16.37 mm and traversed completely through the tumor at a depth of 27.08 mm. For the green tumor, the penetration depth was calculated from 30.31 mm to 40.48 mm, representing the depth at which the needle contacted the surface of the tumor to the depth at which the needle completely traversed the tumor. A best fit equation is obtained by applying polynomial fit to the data on MATLAB using the *polyfit()* function as discussed in the section 3.4.1, further explaining the dynamics of this relationship. Equations for the fabricated tumors inside the phantom were derived by analyzing the points of contact on the curve representing the entry and exit point of the blue and green tumors. For the fabricated ecoflex 30 (blue) tumor, the relationship is described by the equation below, where x represents the depth (mm) and y denotes the force (N):

$$y = 0.0058443x^2 - 0.16837x + 1.2893 \tag{4.2}$$

and for the ecoflex 50 (green) tumor, it is:

$$y = 0.011696x^2 - 0.61478x + 8.399 \tag{4.3}$$

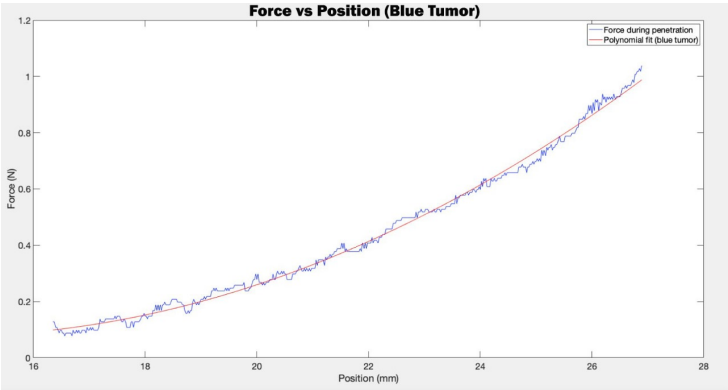

Figure 4.12: Polynomial fit for the ecoflex 30 (blue) tumor in the gelatin phantom

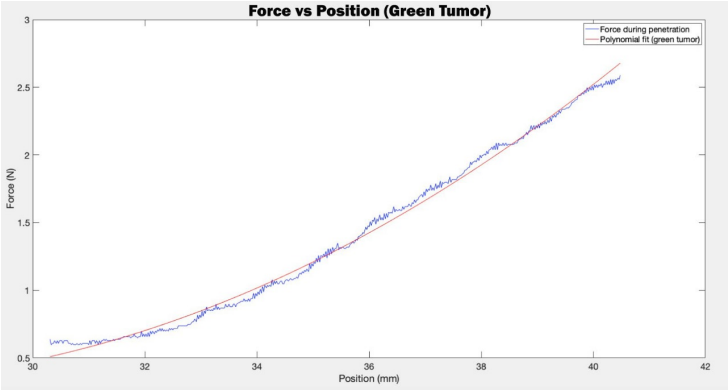

Figure 4.13: Polynomial fit for the ecoflex 50 (green) tumor in the gelatin phantom

The derivatives of the aforementioned equations were computed to evaluate the rate of change of the force in relation to the depth. This is represented by the slope of the equations at a specific depth, as depicted

in Figure 4.14. To enable a clear comparison, identical penetration depths were considered for both tumors. This penetration depth is considered at the point at which the needle first interacts with the phantom. The derivatives for the blue and green tumors are detailed below:

$$y' = 0.0116886x - 0.16837$$

and

$$y' = 0.023392x - 0.61478$$

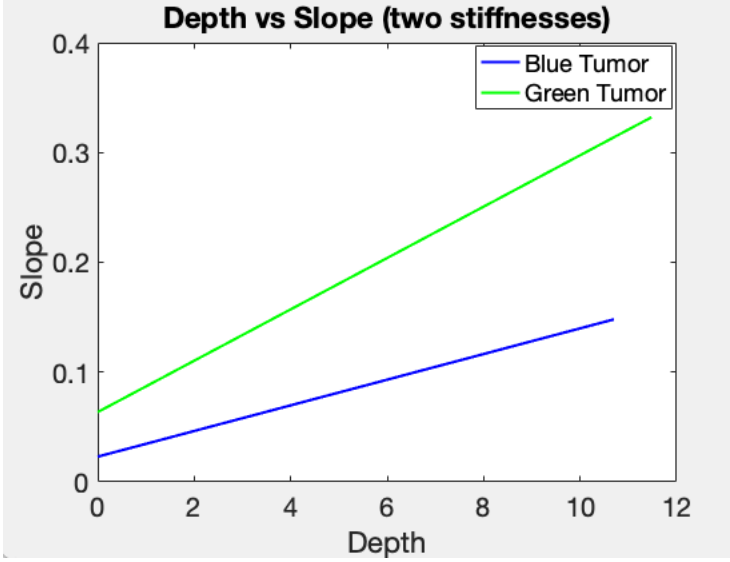

Figure 4.14: Slope-Penetration depth relationship for blue and green tumors in the phantom

To analyze the interaction forces for the healthy tissue, needle insertion through healthy tissue (gelatin phantom that mimics the properties of healthy tissue) was performed. Figure 4.15 shows the force vs. time graphs for needle insertion in healthy tissue and two different tumor stiffnesses. The force required for needle insertion in healthy tissue (gelatin) is relatively constant, with a mean force of 0.1104 N.

Furthermore, the frictional forces obtained from this experiment are correlated with the theoretical model derived from the modified Karnopp model, as referenced in 3.4.2. In this model, only dynamic friction is considered based on the control parameters from the test setup. Given that both velocity and depth remain constant, and the velocity is positive (since

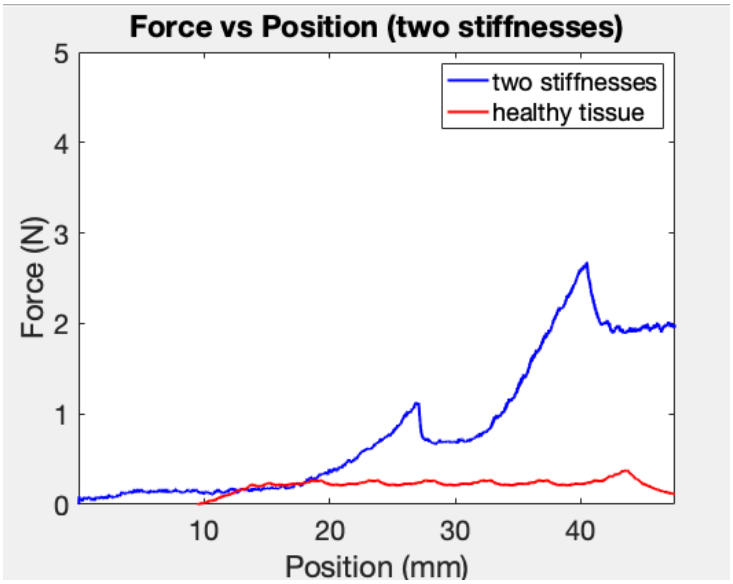

Figure 4.15: Force vs. time graphs for needle insertion into healthy tissue, both with and without tumors exhibiting varied mechanical properties.

only the needle insertion phase is considered), the frictional force can be determined using the fourth relation from the modified Karnopp model, where $\dot{z} \geq \Delta v/2$:

$$F_{\text{frictional}} = C_p + 2.772 * b_p; \tag{4.4}$$

The section 4.16 shows the experimental data as well as the theoretical modelled data of the frictional forces. In the modeling process, only data with a specified relative velocity is utilized to determine the coefficients for dynamic friction and damping. For modelling the forces, data with specific relative velocity is used to determine the dynamic friction and damping coefficient. The frictional force after the penetration through ecoflex 30 (blue) is 0.6905 N, while after the penetration through ecoflex 50 (green) it is 1.9328 N.

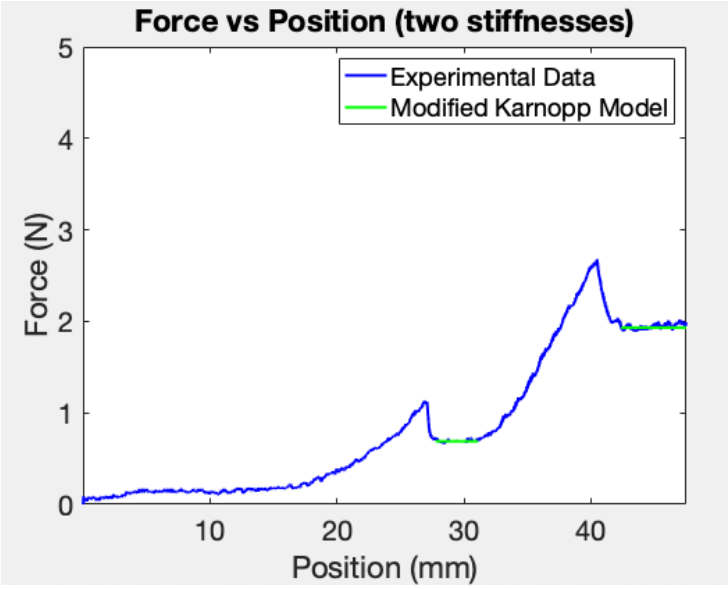

Figure 4.16: Experimental and theoretical analyses using the modified Karnopp model to evaluate frictional forces, as depicted in the Force vs. time graphs for needle insertion.

Chapter 5

Discussion

This section delves into the evaluation and results derived from experiments conducted with the 1-DOF needle insertion robotic device on the two phantoms.

5.1 Design Evaluation Results

The initial tests were centered on understanding the forces that influence the needle. The two forces, clamp force and needle support frictional force were calculated using the equation 3.1. Due to the design specifications, the force at the clamp was calculated to be less than the anticipated requirement. The force was recorded at 1.082 N, which is 15% below the 10 N maximum load as per the set requirement. This value includes all design forces, including friction, and not just the clamp forces. A small fraction of this 10 N is attributed to the clamp joint. By doing so, the forces can be concentrated solely on needle-tissue interactions, thereby enhancing their efficiency. Another design-induced force affecting the needle comes from the support. In addition to this, the designs forces here 1.3155 N was also calculated to be less than 15% of 10N, underscoring its minimal impact on needle-tissue forces. Both of these forces were determined using the equation provided in the previous section 3.1. The forces were measured three times for the experiments, and the low standard deviation which is 0.0319 N calculated shows that the results were consistent and close to the mean of the forces. The efficiency of the needle-tissue interaction forces was improved by optimizing the impact of the design forces and reducing its noise.

5.2 Results of the Needle insertion through the fabricated tumors

Experiments were conducted on the fabricated tumors to assess their material stiffness during needle penetration. With the same experimental setup and conditions, the peak force values calculated show that a steeper curve in the green tumor which is 1.96 N indicates higher stiffness, while a more gradual curve for the blue tumor suggests lower stiffness with 1.44 N. This difference highlights the distinct mechanical properties of the ecoflex 30 and 50 materials. The ecoflex 50 (green tumor) demonstrates greater stiffness, as supported by the data in Table 3.2. During needle penetration, the force rose exponentially due to cumulative compression, strain, and increasing frictional forces. This exponential increase in force is primarily attributed to stiffness, and friction, detailed in section 3.4. While, it was observed that cutting forces remain consistent. However, it's crucial to note that cutting does not occur continuously throughout the procedure. Sometimes, there's no cutting happening, which could mean the needle is either not moving or there's other forces acting on it.

5.3 Results of the Needle insertion in Ecoflex phantom

The experimental findings demonstrated the depth of the needle's penetration into the tumor. During these experiments, the needle was inserted into one tumor inside the ecoflex phantom in both of the cases. The successful piercing of the ecoflex 30 (blue tumor) is evident in Figure 4.7b. Upon contact, there's an initial peak in force, which then sharply rises, leading to a higher overall force. However, for the ecoflex 50 (green tumor) it can be seen in Figure 4.8b that there are additional peaks and stiffness forces to the data. Contrary to the assumption that the needle follows a perfectly straight trajectory during insertion, there were minor deflections as it traversed the tissue. These deflections, potentially arising from factors such as tissue heterogeneity or needle-tissue interactions, can influence the recorded force. While it should be noted that both the tumors were pierced, the peak stiffness was calculated during the exit of needle tip from the tumor, where the green tumor required a considerably higher stiffness force of 5.57 N, and the blue tumor required a force of 2.53 N. The incline of the force-versus-depth curve in Figures 4.7 and 4.8 serves as an indicative metric for discerning material characteristics of the two materials (ecoflex 30 and 50).

The noise observed in the force readings, can be attributed to the fact that the phantom was held by hand for support during these two experiments. Tissues of varying stiffness begin to deform even before the needle makes contact with the tumor. As, a result the force dynamics and penetration behavior can vary significantly based on the inherent stiffness and structural properties of the tumor being targeted. This emphasizes the significance of a detailed understanding when selecting needle types and formulating insertion strategies for diverse tumor types.

5.4 Results of the Needle insertion in Gelatin phantom

To mitigate the stickiness of the ecoflex phantom, a gelatin phantom was introduced, as discussed in section 4.5. This phantom explains the needle's interaction with both the blue and green tumors. Notably, the gelatin phantom's healthy tissue was more penetrable than the ecoflex's, attributed to the latter's adhesive and opaque nature, addressing a research question from section 1.3. The force measurements, obtained from needle insertions into tumors with varying stiffness levels, were utilized to develop and refine the needle-tissue force models discussed in 3.4. Figure 4.15 illustrates the minimal forces on the healthy gelatin tissue. These minimal forces were neglected when modeling the needle's interaction with the fabricated tumors. It was assumed that cutting forces primarily exist during the needle's exit and remain consistent, as supported by [3]. This uniformity indicates that the needle's main interaction with the tumor occurs during its exit, effectively combining the entry and exit phases. Force-depth graphs in Figures 4.12 and 4.13 offer insights into the needle's interaction with liver phantom tissues of distinct stiffness. In order to model the stiffness force ($F_{\text{stiffness}}$), polynomial fit was applied to the force vs insertion depth, as seen in section 3.4, yield predictive models for future needle insertions, enhancing comprehension of force dynamics across liver tissue regions. The polynomial equation coefficients for ecoflex 50 (green tumor) highlight the green tumor's heightened stiffness compared to the blue, corroborated by Table 3.2 (where the coefficient of $\hat{a2}$ is 0.01169 N/mm for ecoflex 50 while for ecoflex 30 it is 0.0058443 N/mm).

In Figures 4.15 and 4.4, a consistent observation is noted: as the needle advances deeper into the phantom's healthy tissue (gelatin), the force remains largely invariant. This behavior implies a relatively low stiffness for gelatin.

The predominant force during this interaction appears to be the cutting force, which consistently averages at approximately 0.1104 N, suggesting a uniform resistance from the gelatin across its depth. For modeling the frictional forces post-tumor penetration, the modified Karnopp model is used from the section 4.4. Given the constant velocity in relation to depth and the needle's surface area during penetration, it can be inferred that frictional forces are calculated to be constant. Therefore, the damping observed post-penetration through the blue and green tumors remains consistent, as illustrated in Figure 4.16. The behaviour of the frictional forces was calculated based on the coefficients of Cp (dynamic friction) and bp (damping coefficient). It is important to validate this experimental observations with the mathematical model. The damping post-penetration through the green tumor is observed to be 2.7 times greater than that after the blue tumor, indicating a significantly higher stiffness for the green tumor which can be observed from the 3.2 as well.

5.5 Collaborative Insights

The design of the 1-DOF robotic needle insertion device helped in evaluating a haptic system, as illustrated in Figure 5.1. A haptic device was designed to evaluate the performance of rPAM actuators [48] in Minimally Invasive Surgery (MIS), particularly for needle insertions into soft tissue. This haptic device controls a slave device; when the haptic device is maneuvered in a single Degree of Freedom (1 DoF), the needle responds in kind. The forces encountered by the needle on the slave side are recorded and juxtaposed with the forces applied by the user on the haptic device. As the forces on the slave side intensify, the air pressure on the haptic device is augmented, ensuring that the haptic device user feels forces analogous to those experienced by the needle. The incorporation of the slave configuration, recognized as a fundamental element of the design methodology, has been instrumental in helping enhance the capabilities of the haptic system.

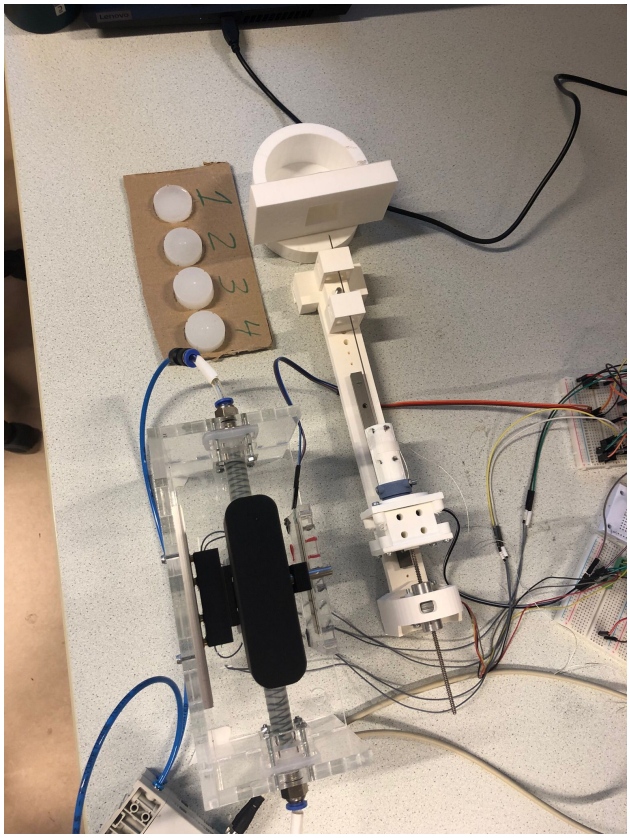

Figure 5.1: Haptic Setup [49]

Chapter 6

Conclusion and Future Work

6.1 Conclusion

The study explored the complexities of incorporating force sensing into a 1-DOF needle insertion robot designed for liver interventions. This 1-DOF robotic mechanism confirms the viability of such integration, emphasizing advancements in tumor detection during liver procedures. The research initially focused on evaluating various tumor detection techniques, understanding their constraints, and examining the latest innovations in needle insertion robotic systems. The literature review indicated that robots equipped with force sensing could offer an addition in reducing the prevalent image-guided methods usage as well as providing more efficiency for detection of the tumors. Furthermore, a liver phantom, which mimics human liver characteristics, was utilized. The primary goal was to showcase the robot's ability to navigate the phantom, identify artificial tumors, and evaluate their firmness. This was achieved by ensuring the robot's operation was straightforward and intuitive.

Addressing the challenge of using force measurements to determine tissue stiffness during a 1-DOF needle insertion procedure in a slave configuration system, this study unveils key insights. The 1-DOF robotic device's development and evaluation are based on the forces exerted on the needle, including design forces and needle-tissue interactions. These forces significantly influence the device's efficiency. The design forces accounted for 15% of the total 10 N load, which is relatively minimal, enhancing the device's accuracy in measuring needle-tissue interactions. Furthermore, experiments showed that the design forces remained consistent across different workspace positions.

Another significant finding from the research was the material composition of the liver phantom, prompting further investigation into its influence on force readings. Experiments with the gelatin and ecoflex phantoms showed distinct force profiles for each material. The gelatin phantom consistently displayed minimal force variations within its healthy tissue, but a discernible spike was observed upon piercing through a fabricated tumor. On the other hand, the ecoflex phantom, with its adhesive properties, presented more subtle force changes. This feedback underscores the method's precision in identifying material transitions, highlighting its potential for enhancing needle insertion techniques.

Furthermore, an experiment with single needle insertion with gelatin phantom was also conducted shown in section 4.11, to see the successive changes in the material and the robotic device was able to successfully detect ecoflex 30 and exoflex 50 present inside healthy tissuse of the phantom. In addition to this, force modeling of the stiffness and frictional forces acting on the needle was also done in order to see the validate it for the experimental results.

In conclusion, the integration of the force measurement in the 1-DOF needle insertion robotic device has successfully enhanced the detection of different materials based on their tissue stiffness. When compared to the existing tumor detection approach, the initial proof of concept and evaluation suggest the possibility of reduced procedure times and a potential decrease in tissue damage, attributed to its precision and consistency. It is evident that this study establishes a foundational framework, directing future endeavours towards the development of effective tumor detection, incorporating real-time force sensing as well as more efficient and precise in the needle insertion robot.

6.2 Recommendations

The 1-DOF needle insertion robotics device can be configured as a slave device in a teleoperation setup controlled by a haptic device. This master-slave configuration would enable the operator to remotely manipulate the needle, providing a sense of touch and feedback. The performance and capabilities of these robotic devices, when used in teleoperations, can be significantly enhanced by integrating tactile and sensory input. A force-torque sensor might be employed to offer additional insights, primarily about needle deflection and alignment, during the operation, especially in

more intricate needle insertion settings. Explorations might include varying speeds of insertion, experimenting with different needle materials, and applying various coatings on the needle surface to minimize friction and noise. Such measures aim to refine the needle insertion process, ensuring a smoother and more consistent procedure.

The current model focused solely on axial forces, distinguishing distinct forces based on practical considerations and time limitations. Hence, a detailed force modeling is still required for a comprehensive understanding of the interactions during needle insertions. As previously highlighted in chapter 5, the physical properties of the phantom used in the experiments, such as texture and uniformity, play a significant role. The needle's penetration through the phantom encounters substantial friction and cutting forces, especially when interacting with the phantom's sticky material. This interaction leads to an exponential increase in resistance against the needle. Recognizing that the phantom's sticky nature amplifies forces not typically present in human livers marks a limitation in this study.

Furthermore, the design of the robotic device could be adapted to accommodate different types of force sensors, with enhancements made to optimize the interface between the sensor and the needle. Future experiments could also involve different sizes and shapes of tumors to further test the versatility and adaptability of the robotic device. Integrating the system with a robotic device that has several degrees of freedom would enable the system to steer the needle by enabling more intricate movements and trajectories. This would open up new possibilities for navigating around to the tumor areas that are challenging to detect. Further developments in the area of robotic-assisted needle insertions will be made possible by these improvements and considerations.

References

1. Jiang, H., Shi, T., Bai, Z. & Huang, L. Ahcnet: An application of attention mechanism and hybrid connection for liver tumor segmentation in ct volumes. *Ieee Access* **7,** 24898–24909 (2019).
2. Anwanwan, D., Singh, S. K., Singh, S., Saikam, V. & Singh, R. Challenges in liver cancer and possible treatment approaches. *Biochimica et Biophysica Acta (BBA)-Reviews on Cancer* **1873,** 188314 (2020).
3. Okamura, A. M., Simone, C. & O'leary, M. D. Force modeling for needle insertion into soft tissue. *IEEE transactions on biomedical engineering* **51,** 1707–1716 (2004).
4. Najarian, S., Fallahnezhad, M. & Afshari, E. Advances in medical robotic systems with specific applications in surgery—a review. *Journal of medical engineering & technology* **35,** 19–33 (2011).
5. Carstensen, E. L., Parker, K. J. & Lerner, R. M. Elastography in the management of liver disease. *Ultrasound in medicine & biology* **34,** 1535–1546 (2008).
6. Masuzaki, R. *et al.* Assessing liver tumor stiffness by transient elastography. *Hepatology international* **1,** 394–397 (2007).
7. Liu, Q. *et al.* Molecular fluorescent probes for liver tumor imaging. *Chemistry–An Asian Journal* **17,** e202200091 (2022).
8. Zhao, Y. *et al.* Influence of three-dimensional visual reconstruction technology combined with virtual surgical planning of CTA images on precise resection of liver cancer in hepatobiliary surgery. *Computational and Mathematical Methods in Medicine* **2022** (2022).
9. Beccani, M., Di Natali, C., Rentschler, M. E. & Valdastri, P. *Wireless tissue palpation: Proof of concept for a single degree of freedom* in *2013 IEEE International Conference on Robotics and Automation* (2013), 711–717.

10. Kemmerer, S. R., Mortele, K. J. & Ros, P. R. CT scan of the liver. *Radiologic Clinics of North America* **36,** 247–261 (1998).

11. Brenner, D. J. & Hall, E. J. Computed tomography—an increasing source of radiation exposure. *New England journal of medicine* **357,** 2277–2284 (2007).

12. Tholey, G., Desai, J. P. & Castellanos, A. E. Force feedback plays a significant role in minimally invasive surgery: results and analysis. *Annals of surgery* **241,** 102 (2005).

13. Cuschieri, A. Whither minimal access surgery: tribulations and expectations. *The American Journal of Surgery* **169,** 9–19 (1995).

14. Moreno-Egea, A. *et al.* Laparoscopic repair of secondary lumbar hernias: open vs. laparoscopic surgery. A prospective, nonrandomized study. *Cirugıéa española* **77,** 159–162 (2005).

15. Aslam, M. S. *et al.* Liver-tumor detection using CNN ResUNet. *Comput. Mater. Contin* **67,** 1899–1914 (2021).

16. Tanaka, H. *Current role of ultrasound in the diagnosis of hepatocellular carcinoma* Mar. 2020. `https://doi.org/10.1007/s10396-020-01012-y`.

17. Duck, F. A. Hazards, risks and safety of diagnostic ultrasound. *Medical engineering & physics* **30,** 1338–1348 (2008).

18. Mauri, G. *et al.* Real-time US-CT/MRI image fusion for guidance of thermal ablation of liver tumors undetectable with US: results in 295 cases. *Cardiovascular and interventional radiology* **38,** 143–151 (2015).

19. *Ultrasound scan for liver cancer — cancerresearchuk.org* `https://www.cancerresearchuk.org/about-cancer/liver-cancer/getting-diagnosed/tests/ultrasound-scan`. [Accessed 15-09-2023].

20. Fred, H. L. Drawbacks and limitations of computed tomography: views from a medical educator. *Texas Heart Institute Journal* **31,** 345 (2004).

21. Choi, E. S., Kim, J. S., Lee, J. K., Lee, H. A. & Pak, S. Prospective evaluation of low-dose multiphase hepatic computed tomography for detecting and characterizing hepatocellular carcinoma in patients with chronic liver disease. *BMC Medical Imaging* **22,** 1–11 (2022).

22. Monfaredi, R., Cleary, K. & Sharma, K. MRI robots for needle-based interventions: systems and technology. *Annals of biomedical engineering* **46,** 1479–1497 (2018).

23. Salomonowitz, E. MR imaging-guided biopsy and therapeutic intervention in a closed-configuration magnet: single-center series of 361 punctures. *American Journal of Roentgenology* **177,** 159–163 (2001).

24. Langen, H.-J., Kugel, H. & Landwehr, P. MR-guided core biopsies using a closed 1.0 T imager. First clinical results. *European journal of radiology* **41,** 19–25 (2002).

25. Das, C. J., Goenka, A. H. & Srivastava, D. N. MR-guided abdominal biopsy using a 1.5-Tesla closed system: a feasibility study. *Abdominal imaging* **35,** 218–223 (2010).

26. Yang, C., Xie, Y., Liu, S. & Sun, D. Force modeling, identification, and feedback control of robot-assisted needle insertion: a survey of the literature. *Sensors* **18,** 561 (2018).

27. Yang, T. *et al. Force feedback control of a robotic needle insertion into layered soft tissues* in *2018 25th international conference on mechatronics and machine vision in practice (M2VIP)* (2018), 1–5.

28. Washio, T. & Chinzei, K. *Needle force sensor, robust and sensitive detection of the instant of needle puncture* in *Medical Image Computing and Computer-Assisted Intervention–MICCAI 2004: 7th International Conference, Saint-Malo, France, September 26-29, 2004. Proceedings, Part II 7* (2004), 113–120.

29. Zhang, S., Qiao, P., Huang, Z., Xia, C., *et al. Needle-tissue interaction force study during simulated regional anaesthesia* in *Journal of Physics: Conference Series* **1544** (2020), 012064.

30. Rossa, C., Lehmann, T., Sloboda, R., Usmani, N. & Tavakoli, M. A data-driven soft sensor for needle deflection in heterogeneous tissue using just-in-time modelling. *Medical & biological engineering & computing* **55,** 1401–1414 (2017).

31. Lehmann, T., Rossa, C., Sloboda, R., Usmani, N. & Tavakoli, M. *Needle path control during insertion in soft tissue using a force-sensor-based deflection estimator* in *2016 Ieee International Conference on Advanced Intelligent Mechatronics (Aim)* (2016), 1174–1179.

32. Tucan, P. *et al.* Design and Experimental Setup of a Robotic Medical Instrument for Brachytherapy in Non-Resectable Liver Tumors. *Cancers* **14,** 5841 (2022).

33. Torres, D. M. & Harrison, S. A. Diagnosis and therapy of nonalcoholic steatohepatitis. *Gastroenterology* **134,** 1682–1698 (2008).

34. Bugianesi, E. *et al.* Expanding the natural history of nonalcoholic steatohepatitis: from cryptogenic cirrhosis to hepatocellular carcinoma. *Gastroenterology* **123,** 134–140 (2002).

35. Hui, A. *et al.* Histological progression of non-alcoholic fatty liver disease in Chinese patients. *Alimentary pharmacology & therapeutics* **21,** 407–413 (2005).

36. Angulo, P. Nonalcoholic fatty liver disease. *New England Journal of Medicine* **346,** 1221–1231 (2002).

37. Ludwig, J., Viggiano, T. R., Mcgill, D. B. & Oh, B. *Nonalcoholic steatohepatitis: Mayo Clinic experiences with a hitherto unnamed disease.* in *Mayo Clinic Proceedings* **55** (1980), 434–438.

38. Mueller, S. & Sandrin, L. Liver stiffness: a novel parameter for the diagnosis of liver disease. *Hepatic medicine: evidence and research,* 49–67 (2010).

39. Banovac, F. *et al. Liver tumor biopsy in a respiring phantom with the assistance of a novel electromagnetic navigation device* in *Medical Image Computing and Computer-Assisted Intervention—MICCAI 2002: 5th International Conference Tokyo, Japan, September 25–28, 2002 Proceedings, Part I 5* (2002), 200–207.

40. He, L., Herzig, N., de Lusignan, S. & Nanayakkara, T. *Granular jamming based controllable organ design for abdominal palpation* in *2018 40th Annual International Conference of the IEEE Engineering in Medicine and Biology Society (EMBC)* (2018), 2154–2157.

41. Kondo, T., Kitatuji, M. & Kanda, H. *New tissue mimicking materials for ultrasound phantoms* in *IEEE Ultrasonics Symposium, 2005.* **3** (2005), 1664–1667.

42. Scali, M., Veldhoven, P. A., Henselmans, P. W., Dodou, D. & Breedveld, P. Design of an ultra-thin steerable probe for percutaneous interventions and preliminary evaluation in a gelatine phantom. *PloS one* **14,** e0221165 (2019).

43. Basdogan, C. in *Soft Tissue Biomechanical Modeling for Computer Assisted Surgery* 229–241 (Springer, 2012).

44. De Jong, T. L. *et al.* PVA matches human liver in needle-tissue interaction. *Journal of the mechanical behavior of biomedical materials* **69,** 223–228 (2017).

45. Wolf, D. C. Evaluation of the size, shape, and consistency of the liver. *Clinical Methods: The History, Physical, and Laboratory Examinations. 3rd edition* (1990).

46. Ndi Digital. *Aurora Tools* https://www.ndigital.com/electromagnetic-tracking-technology/aurora/aurora-tools/. (Accessed on 23/07/2023).

47. *Ecoflex™ 00-30 Product Information — smooth-on.com* https://www.smooth-on.com/products/ecoflex-00-30/. [Accessed 24-08-2023].

48. Skorina, E. H. *et al.* Reverse pneumatic artificial muscles (rPAMs): Modeling, integration, and control. *PloS one* **13,** e0204637 (2018).

49. *Design and implementation of a haptic device for needle insertion — Robotics and Mechatronics — ram.eemcs.utwente.nl* https://www.ram.eemcs.utwente.nl/education/assignments/design-and-implementation-haptic-device-needle-insertion. [Accessed 02-10-2023].